ADVANCED ENERGY MATERIALS

FULL PAPER

Lithium-Ion Batteries

ADVANCED
ENERGY
MATERIALS

www.advenergymat.de

Ion Transport Nanotube Assembled with Vertically Aligned Metallic MoS₂ for High Rate Lithium-Ion Batteries

Yucong Jiao, Alolika Mukhopadhyay, Yi Ma, Lei Yang, Ahmed M. Hafez, and Hongli Zhu*

Metallic phase molybdenum disulfide (MoS_2) is well known for orders of magnitude higher conductivity than 2H semiconducting phase MoS_2. Herein, for the first time, the authors design and fabricate a novel porous nanotube assembled with vertically aligned metallic MoS_2 nanosheets by using the scalable solvothermal method. This metallic nanotube has the following advantages: (i) intrinsic high electrical conductivity that promotes the rate performance of battery and eliminates the using of conductive additive; (ii) hierarchical, hollow, porous, and aligned structure that assists the electrolyte transportation and diffusion; (iii) tubular structure that avoids restacking of 2D nanosheets, and therefore maintains the electrochemistry cycling stability; and (iv) a shortened ion diffusion path, that improves the rate performance. This 1D metallic MoS_2 nanotube is demonstrated to be a promising anode material for lithium-ion batteries. The unique structure delivers an excellent reversible capacity of 1100 mA h g^{-1} under a current density of 5 A g^{-1} after 350 cycles, and an outstanding rate performance of 589 mA h g^{-1} at a current density of 20 A g^{-1}. Furthermore, attributed to the material's metallic properties, the electrode comprising 100% pure material without any additive provides an ideal system for the fundamental electrochemical study of metallic MoS_2. This study first reveals the characteristic anodic peak at 1.5 V in cyclic voltammetry of metallic MoS_2. This research sheds light on the fabrication of metallic 1D, 2D, or even 3D structures with 2D nanosheets as building blocks for various applications.

1. Introduction

As a promising 2D material for energy storage and conversion, molybdenum disulfide (MoS_2) has attracted extensive attention recent years due to its unique layered structure and good electrochemical performances on battery storage and supercapacitors.[1–5] MoS_2 exhibits three phases: semiconducting (2H) phase and metallic phase (1T and distorted 1T′ phase). Semiconducting trigonal 2H MoS_2 material has been proved to be a promising anode material for lithium-ion batteries due to its high theoretical specific capacity (670 mA h g^{-1}, much higher than commercial graphite (372 mA h g^{-1})) and low cost.[6,7] However, the structural deterioration during cycling caused by the large volume change and the poor intrinsic conductivity with a direct bandgap of ≈1.9 eV significantly inhibits the further applications of 2H MoS_2 on lithium-ion batteries.[8,9] One of the best and typical strategies to ameliorate the structural stability and electrical conductivity of MoS_2 based anode is to fabricate hybrid 2H MoS_2 nanocomposites with conductive carbonaceous materials, such as carbon fibers, graphene, and carbon nanotubes. These hybrid MoS_2-carbon nanocomposites (MCNs) could deliver a decent capacity of ≈900 mA h g^{-1} at 1 A g^{-1} current density on lithium-ion batteries for 100 cycles.[2,10,11] Unfortunately, this strategy also induces new constraints to the MCNs' applications on lithium-ion batteries, such as reducing the mass loading of MoS_2, consuming more electrolytes, raising the electrode cost, and increasing the reaction barrier between lithium-ion and MoS_2.[12] Even though carbon source can improve the conductivity of the electrode, the intrinsic insulating property of 2H MoS_2 remains unchanged, which will significantly limit its rate performance and impede the utilization of the active MoS_2.

Recently, the metastable metallic phase (1T or 1T′) MoS_2 has emerged with promising potential on lithium-ion storage field. As reported,[8,13–15] benefited from its different Mo and S atom coordination of octahedral structure with dense intercalation sites, metallic phase MoS_2 owns five orders of magnitude higher electrical conductivity than that of 2H MoS_2. This high intrinsic conductivity will be beneficial for the performance of metallic MoS_2 electrode in the following two aspects. On one hand, pure metallic MoS_2 can be directly applied as an anode electrode on lithium-ion batteries without adding any conductive carbon sources, which would facilitate the electrochemical storage fundamental mechanism studying of metallic MoS_2. On the other hand, the utilization of active MoS_2 can also be maximized, and the lithium-ion charge/discharge capacity could be tremendously enhanced at high current density, therefore intensely improves the rate performance as well as the reversible capacity of metallic MoS_2 as an anode electrode. However, the conventional preparation methods of metallic MoS_2 by alkali metal intercalation and exfoliation are complicated, unstable, and dangerous.[13] Recent reports provided several new strategies to prepare metallic MoS_2 by solvothermal method,[9,16,17] which stabilized the metallic MoS_2 by interlayer

Dr. Y. Jiao, A. Mukhopadhyay, Y. Ma, L. Yang, A. M. Hafez, Prof. H. Zhu
Department of Mechanical and Industrial Engineering
Northeastern University
Boston, MA 02115, USA
E-mail: h.zhu@neu.edu

ADVANCED
SCIENCE NEWS
www.advancedsciencenews.com
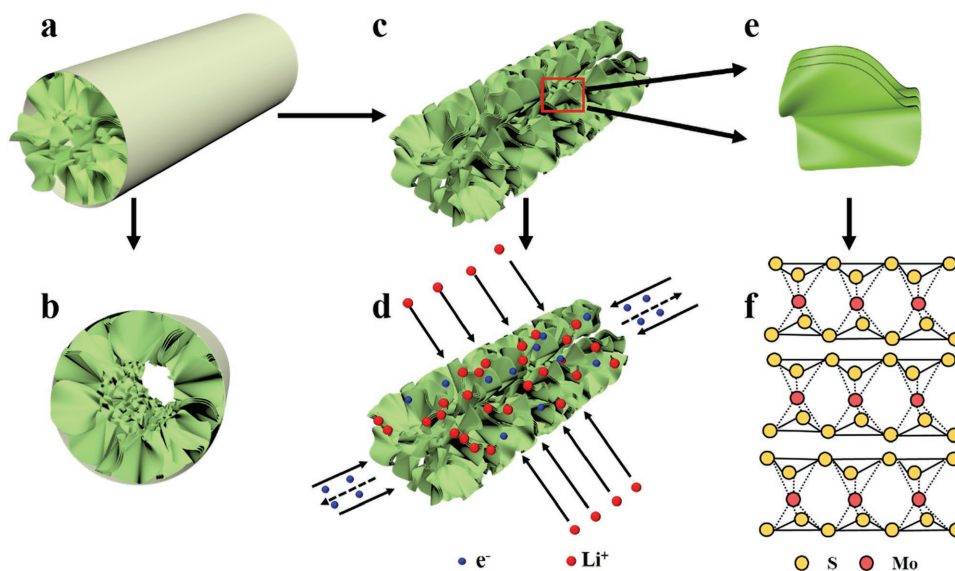
ADVANCED
ENERGY
MATERIALS
www.advenergymat.de

Figure 1. Schematic representation of metallic MoS_2 nanotube structure. a) Metallic MoS_2 nanosheets vertically grown on the internal wall of AAO tube. b) Metallic MoS_2 nanotube in the template, showing the tubular hollow structure. c) Metallic MoS_2 nanotube after etching of template. d) Porous metallic MoS_2 nanotube. The red dots represent lithium-ion and the blue dots represent electron. e) Building blocks of layered metallic MoS_2 nanosheets. f) Octahedral atom structure of metallic MoS_2. The yellow dots are representing S atom and the red dots representing Mo atom.

insertion of guest ions, such as NH_4^+.[17] However, all above-mentioned metallic MoS_2 was further mixed with conductive carbon sources, including carbon fiber cloth,[9] single-walled carbon nanotube films,[16] and graphene frame,[17] for applications on supercapacitor or battery. Additionally, *N, N*-dimethylformamide (DMF) was employed as solvent in all of these papers, which is environmentally harmful.

Based on latitude mentioned above, in this study, we developed a novel and facile approach to fabricate carbon-free, porous nanotube with 2D metallic MoS_2 nanosheets as building blocks by solvothermal method with ethanol as solvent. This is the first time demonstration of stable conductive MoS_2 nanotube fabricated in ethanol, which is more environment-friendly and low-cost, compared to DMF. Also, the unique nanotube structure possesses significant advantages on avoiding aggregation of MoS_2 nanosheets, benefitting electrolyte transportation, shortening lithium-ion diffusion path, and optimizing intercalation sites.[12,18,19] Therefore, this intercalation sites riched, porous 1D nanotube structure delivers high rate lithium-ion charge/discharge performance and enhanced structural and cycling stability on lithium-ion battery applications with an excellent reversible capacity of 1100 mA h g^{-1} under a current density of 5 A g^{-1} for more than 350 cycles, and an outstanding rate performance of 589 mA h g^{-1} under a current density of 20 A g^{-1}.

2. Results and Discussion

In order to better investigate the intrinsic properties of metallic MoS_2 for fundamental studies on lithium-ion battery, herein, we adopted a simple solvothermal method to fabricate a pure conductive and porous nanotube made from metallic MoS_2 with no additive and binder for lithium-ion battery anode electrode. The

synthesis of metallic MoS_2 nanotube was performed in the environmentally friendly solvent ethanol at low temperature (200 °C) with MoO_3 as Mo source, thioacetamide as S source, and anodic aluminum oxide (AAO) as the template. **Figure 1** shows the schematic representation of the pure metallic MoS_2 nanotube structure. As shown in Figure 1a, the MoS_2 nanosheets are vertically grown on the internal wall of AAO tube and interlaced together. AAO takes two folds of functions here: 1) plays the role as a template and 2) provides support for the metallic MoS_2 nucleation, based on which the metallic MoS_2 grows perpendicularly to the axial direction of tube. Figure 1b is the schematic representation of the as-fabricated MoS_2 in AAO along the longitudinal direction, showing the tubular hollow structure of the metallic MoS_2. After removing the template, the MoS_2 nanotube can still maintain their tubular structure as illustrated in Figure 1c. The as-prepared structure was assembled by multilayered MoS_2 nanosheets (Figure 1e), with their 2D plane vertical to the tube direction and edge exposed to the outside. This unique structural attribute would be beneficial for electrolyte transportation and lithiation/delithiation processes, as shown in Figure 1d. Figure 1f depicts the atomic structure of the layered metallic MoS_2 with octahedral coordination.

The morphology of the MoS_2 nanotube under different magnification was characterized by scanning electron microscopy (SEM) (**Figure 2**). Figure 2a,b shows the low-magnification images of the MoS_2 nanotube, indicating that after the removal of AAO template, the nanotubes still retain their length and tube morphology. This 1D nanotube structure prevents the aggregation, restacking, and structural deterioration of metallic MoS_2 nanosheets, and accommodates the volume changes during MoS_2 cycling on lithium-ion batteries. High-magnification SEM images (Figure 2c,d, and Figure S1, Supporting Information) display the specific porous tubular structure. Figure 2d and Figure S1b (Supporting Information) further confirm the
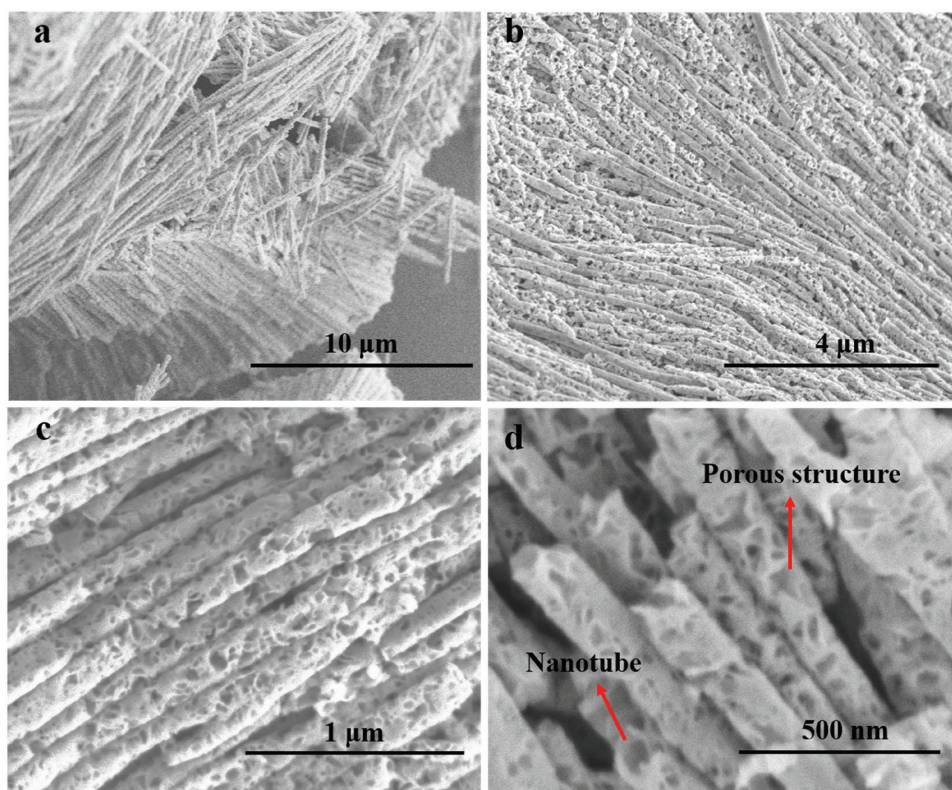
**ADVANCED
SCIENCE NEWS**
www.advancedsciencenews.com

**ADVANCED
ENERGY
MATERIALS**
www.advenergymat.de

Figure 2. a,b) SEM images of the as-prepared MoS$_2$ nanotube under low magnifications. c) High magnification SEM image of MoS$_2$ with clear porous structure. d) SEM image of MoS$_2$ with clear nanotube structure.

nanotube structure of metallic MoS$_2$. This unique structure possesses more advantageous features with sufficient ion transportation tunnels and has been proved to be promising for facilitating rapid electrolyte diffusion as well as shortening lithium-ion diffusion path.[12,18,19] Figure 2d exhibits that the diameter of the as-fabricated tube is around 100 nm, coordinating to the diameter of the AAO tube template.

High-resolution transmission electron microscopy (HRTEM) was also conducted to further investigate the structural attributes of the as-prepared metallic MoS$_2$ nanotube. The existence of a typical flower-like structure of MoS$_2$ on the surface of the nanotubes was evidenced by the low magnification TEM images of the metallic MoS$_2$ nanotubes, as shown in **Figure 3**a and Figure S2 (Supporting Information). Multilayered structure with layer distance of ≈0.71–0.81 nm was explicitly shown in the HRTEM images (Figure 3b,c) The layer distance is larger than typical layer distance in MoS$_2$ (0.62–0.65 nm) due to the interlayer insertion of guest ions arriving from urea and ethanol.[9,17] From Figure 3c,d, we can see the MoS$_2$ edge is exposed to the outside surface, which leads to a conclusion that the nucleation direction of MoS$_2$ is perpendicular to the axial direction of the tube. The layered intercalation sites of the MoS$_2$ are all exposed on the surface of the nanotube, providing great convenience for lithium-ion charge/discharge. In addition, Figure 3a–c exhibits numerous nanopores on the nanotubes, consistent with the SEM results. Consequently, this unique structure can provide more intercalation sites and shorter path ways for lithium-ion intercalation and electrolyte diffusion. The selected area electron

diffraction (SAED) pattern of Figure 3d shows weak and hazy diffraction rings, exhibiting the low crystallinity of the nanotube. Figure 3e–g is the energy dispersive X-ray spectroscopy (EDX) elemental mappings of the as-prepared metallic MoS$_2$ nanotube, showing the same structure feature as Figure 3e. Figure 3f,g confirms that the nanotube is composed of Mo and S elements. More mapping images and the elemental spectrum are also shown in Figure S3 (Supporting Information). Agreeing with the mapping results, the elemental spectrum (Figure S3d, Supporting Information) proves that there are only Mo and S elements in the nanotube structure. The atom arrangement of the metallic MoS$_2$ nanotube was also investigated by HRTEM with the atom distance from A to D of 0.48 ± 0.02 nm, A to B of 0.27 ± 0.02 nm, and A to C of 0.32 ± 0.02 nm (Figure S4, Supporting Information).

Raman spectroscopy (**Figure 4**a), X-ray diffraction (XRD) (Figure 4b), and X-ray photoelectron spectroscopy (XPS) (Figure 4c,d) were performed to identify the phases and chemical composition of the as-prepared MoS$_2$ nanotube. The typical E_g mode at 280 cm^{-1} of the metallic octahedrally coordinated MoS$_2$ is observed from the Raman spectra of the fresh MoS$_2$ sample (Figure 4a). Besides, three additional strong peaks at 146 (J$_1$), 234 (J$_2$), and 333 (J$_3$) cm^{-1} observed in Raman spectrum also confirm the metallic phase of MoS$_2$. The peak at 192 cm^{-1} arises from the different layers of MoS$_2$, and the 372 cm^{-1} peak is supposed to be the E_{2g}^1 peak of 2H MoS$_2$, which may result from the transformation of metallic MoS$_2$ under Raman illumination and freeze drying process

**ADVANCED
SCIENCE NEWS**
www.advancedsciencenews.com

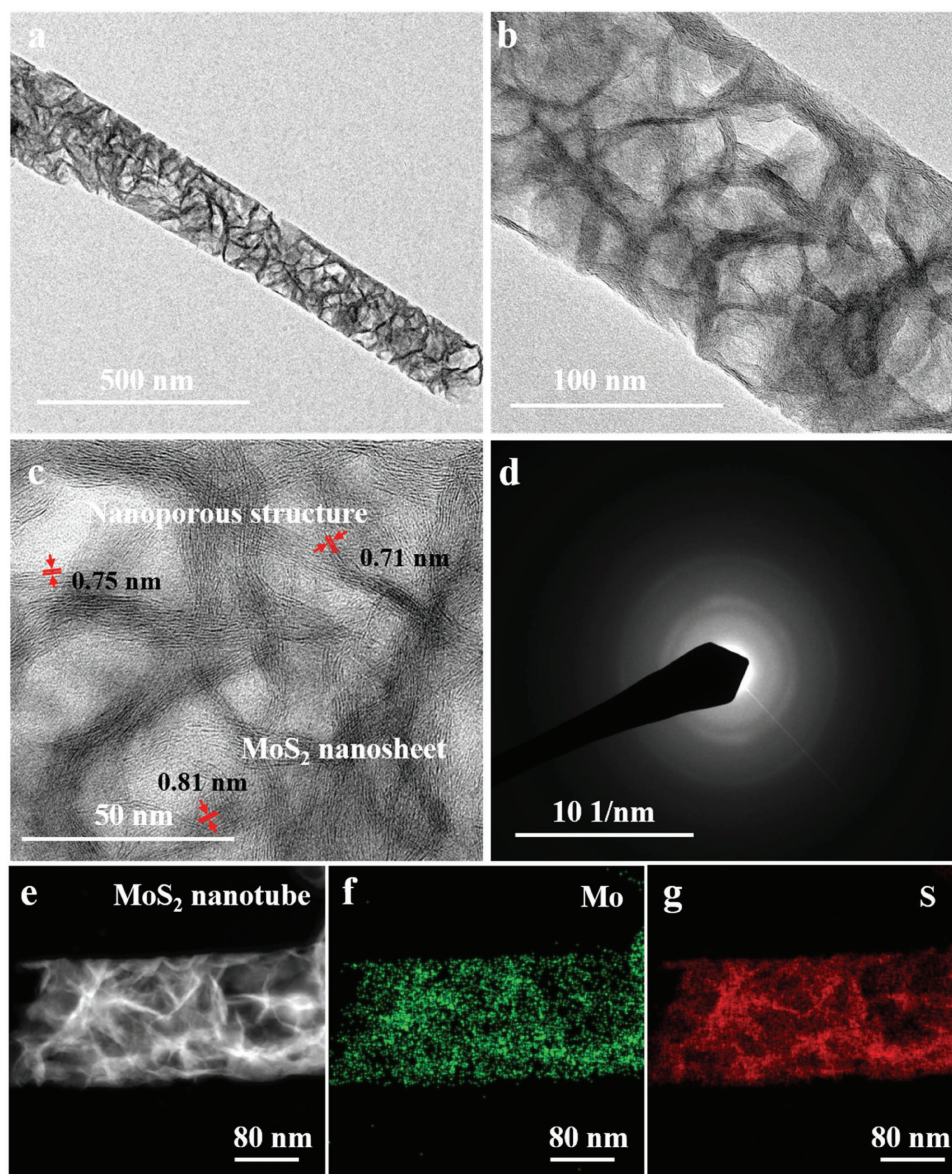**ADVANCED
ENERGY
MATERIALS**
www.advenergymat.de

Figure 3. a) Low-magnification TEM image of the metallic MoS_2 nanotube. b,c) HRTEM images of the as-prepared MoS_2 nanotube under different magnification. d) SAED pattern of the metallic MoS_2 nanotube. e) TEM images of the MoS_2 nanotube. f,g) EDX Mo, S elemental mappings of (e).

of the sample preparation. However, the amount of 2H MoS_2 in metallic MoS_2 nanotube is negligible as the typical A_{1g} peak of 2H MoS_2 at 400 cm^{-1} is nearly vanished. In contrast, the control 2H MoS_2 sample only has two sharp peaks at 372 and 400 cm^{-1} without any additional peaks. In order to further investigate the stability of metallic MoS_2 in air, the Raman spectra of the samples stored in air for 30 and 120 d were also determined. For the sample which was stored in air for 30 d, only a small peak compared to fresh metallic MoS_2 sample at 400 cm^{-1} comes out due to the phase transfer from metallic to semiconducting in air, and the typical peaks for metallic phase of J_1 (146 cm^{-1}), J_2 (234 cm^{-1}), J_3 (333 cm^{-1}) can still be obviously observed. In addition, even after 120 d of air exposure, all the typical peaks for metallic MoS_2 can still be detected, which confirms the exceptional stability of

our metallic MoS_2 sample in air. The underlying mechanism for high stability of metallic tube is that, compared to freely nanosheets, the tubular structure can dramatically reduce the restacking issue. In Figure 4b, XRD pattern (red curve) shows three diffraction peaks at around 10°, 32°, and 58°, attributable to the (002), (100), and (110) planes of the metallic MoS_2. The 2H MoS_2 curve (black curve) owns a different (002) peak position, which is at around 14°, compared to metallic MoS_2.[6,20] Figure 4c,d displays the XPS patterns of the metallic MoS_2 nanotube and 2H MoS_2. The Mo XPS spectra of metallic MoS_2 nanotube consists of two signals at 228.7 and 231.9 eV, which are corresponding to the 3d5/2 and 3d3/2 components of Mo-S bonding in metallic MoS_2, respectively. For the 2H MoS_2 sample, the XPS peaks of Mo are at 229.4 and 232.5 eV, which are ≈0.7 eV higher than the corresponding metallic MoS_2
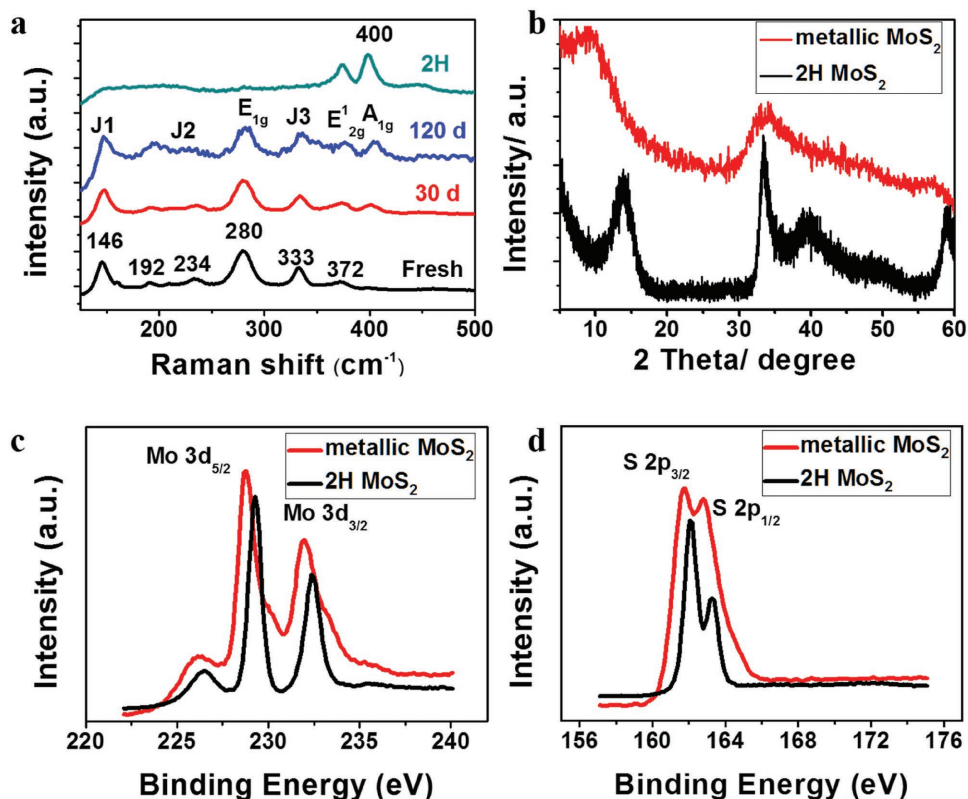
Figure 4. a) Raman patterns of the metallic MoS_2 nanotube of fresh sample, sample after 30 d in air, sample after 120 d in air, and 2H MoS_2 nanosheets. b) X-ray diffraction spectra of the metallic MoS_2 nanotube and 2H MoS_2 nanosheets. c,d) X-ray photoelectron spectroscopy spectra of Mo 3d c) and S 2p d) of the metallic MoS_2 nanotube and 2H MoS_2 nanosheets.

peaks. The XPS signals of S 2p are at 161.6 and 162.8 eV, corresponding to S 2P3/2 and 2P1/2 components, which proved the structure of the material as Mo-S. These S 2p peaks are also ≈0.7 eV lower than the peaks in 2H MoS_2, which are at 162.3 and 163.4 eV, respectively.[8]

In order to further investigate its application value, the as-prepared metallic MoS_2 nanotube was evaluated as an anode material for lithium-ion batteries. To have a pure study system, the batteries were assembled directly without adding any carbon conductive sources and binders. Similarly, the 2H MoS_2 nanosheets batteries were also assembled without any conductive additives and binders. (The corresponding SEM and TEM images of 2H MoS_2 nanosheets could be found at Figure S5, Supporting Information.) Cyclic voltammetry (CV) measurements were first carried out between 0.001 and 3.0 V at 0.2 mV s^{-1} scan ramp to study the lithium-ion storage mechanism of the metallic MoS_2 nanotube. **Figure 5**a shows the CV curves of 1st, 2nd, and 5th cycles of metallic MoS_2 nanotube and the 1st CV cycle of 2H MoS_2 (black curve). The first discharge of the 2H MoS_2 exhibits two peaks at 0.94 and 0.4 V. In detail, the peak at 0.94 V is attributed to the intercalation of lithium-ion into the 2H MoS_2 layer, forming Li_xMoS_2, with the phase transformation of trigonal prisms (2H) to octahedral (1T or 1T') structure.[2,11,21,22] The peak at 0.4 V is ascribed to the conversion from Li_xMoS_2 to Li_2S and Mo nanoparticles.[2,23] During the first delithiation process (anodic scan), predicted peak around 1.5 V in 2H MoS_2 owing to the lithium-ion

association with Mo reduction is absent.[21] Only one distinct peak appears at 2.4 V, corresponding to the oxidation of Li_2S to sulfur.[24] In contrast, no peaks are observed at around 0.94 V during the first cathodic scan of metallic MoS_2, which indicates that no phase transformation from 2H to metallic occurred during the intercalation of lithium-ion into MoS_2 layer.[9] The absence of the phase transformation peaks further identifies our as-prepared material as pure metallic MoS_2. In the first anodic scan of metallic MoS_2, two remarkable peaks are present at 1.5 and 2.3 V, which are assigned to the oxidation of Mo to MoS_2, and the oxidation of Li_2S, respectively.[10,11] In the subsequent discharge cycle, two small reduction peaks appear at 1.25 and 1.5 V, corresponding to the Mo oxidation peak at 1.5 V. The wide peak at 1.8 V is ascribed to the sulfur reduction, which is in good agreement with the conversion from sulfur to polysulfides and then Li_2S.[10] Moreover, the peak at 0.4 V disappears, indicating permanent structural change during the first cycle.[25] The 2nd and 5th cycle curves are nearly overlapped, which reflects the excellent cycling stability of metallic MoS_2 nanotube on lithium-ion storage. However, the peak at 1.5 V in all the charge scan curves of metallic MoS_2 in Figure 5a is significantly different compared to the 2H MoS_2 Li-ion battery curve. This noticeable difference can be explained by the atomic structure of MoS_2. According to the previous reports,[15,22,26] 2H MoS_2 owns a trigonal prisms structure, where the Mo atoms are all surrounded by S atoms. On the contrary, metallic MoS_2 is octahedral structure, with the Mo atoms exposed outside,
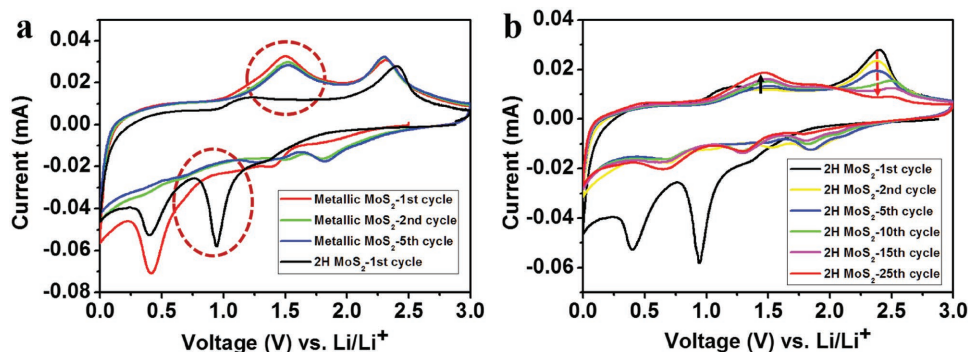
ADVANCED
SCIENCE NEWS
www.advancedsciencenews.com

ADVANCED
ENERGY
MATERIALS
www.advenergymat.de

Figure 5. CV measurements of the metallic MoS_2 nanotube and 2H MoS_2 nanosheets at a scan rate of 0.2 mV s^{-1}. a) The 1st, 2nd, and 5th CV cycle of metallic MoS_2, and the 1st cycle of 2H MoS_2. b) CV curves of 2H MoS_2 at different cycle number.

which is also the reason for the much higher conductivity of metallic MoS_2 than 2H MoS_2. Because of this difference in atomic structure, we assume that it is much easier for the Mo atom in metallic MoS_2 structure to react with lithium-ion during the cathodic scan and get oxidation in the anodic scan, which displayed as the remarkable peak on the CV curve. To further confirm our conclusion, we explored the CV performance of 2H MoS_2 under 25 cycles. Figure 5b shows the 1st, 2nd, 5th, 10th, 15th, 20th, and 25th cycles of 2H MoS_2 battery at a scan rate of 0.2 mV s^{-1}. From the second cycle, the intensity of the reduction peak at 1.8 V (corresponding to the sulfur reduction) decreases continuously with cycling. The same phenomenon happens at the oxidation peak of 2.3 V, because of the sulfur depletion during cycle.[24] On the contrary, the anodic peak at 1.5 V starts to appear from the 2nd cycle, and the intensity of this peak continuously increases with cycling. This could also be explained by the structural change and phase transformation. With the redox reaction during cycling, the phase of 2H MoS_2 gradually transfers to metallic phase, and more Mo atom begins to be involved in the redox reaction with lithium. Accordingly, the reaction peak for Mo atom at around 1.25 V, and oxidation peak at 1.5 V for Mo turn to be much more intensive. For metallic MoS_2 anode material, the redox reaction of Mo is much distinct compared to 2H MoS_2, since all the Mo atoms are exposed to lithium and electrolyte from the very beginning. Exhibited on CV curves of Figure 5a, the reduction peak at around 1.5 V (Mo atom owns two reduction peaks at 1.24 and 1.5 V according to the literature),[10] and oxidation peak at 1.5 V are both more intensive than 2H MoS_2. We conclude that the peak at 1.5 V in charge scan curve is the typical CV peak for metallic MoS_2 on lithium-ion battery. To the best of our knowledge, this is the first time to highlight the occurrence and importance of the peak at 1.5 V on the anodic scan of metallic MoS_2 lithium battery CV curve.

Figure 6a shows the galvanostatic charge and discharge curves for metallic MoS_2 electrode at a current density of 5 A g^{-1} with a cutoff voltage window of 0.001–3.0 V versus Li$^+$/Li for the first three and 100th, 200th, 300th cycles. The initial discharge and charge capacities are 1414 and 962 mA h g^{-1}, along with a first Coulombic efficiency of 68%, which is caused by the irreversible formation of solid–electrolyte interface film. The voltage plateau at 0.4 V on the 1st discharge curve can be attributed to the conversion of Li$_x$MoS$_2$ to Li$_2$S and Mo nanoparticles,

which is in line with the CV curves of Figure 5a. Accordingly, this plateau is also absent on the subsequent discharge curves because of the permanent structural changes. On the first three charge cycles, there are two plateaus at around 1.5 and 2.4 V, arising from the oxidation of Mo atoms and Li$_2$S compounds that can also be observed on the CV curves. The plateau at 2.4 V of the charge curve disappeared after 100 cycles, because of the depletion of sulfur during cycling, which is also in accordance with the CV results. The discharge and charge curves of the 100th and 200th cycles are nearly overlapped, indicating excellent cycling stability during the process. However, the capacity increases at 300 cycles, which may be caused by the reversible formation of organic polymeric/gel-like layer by electrolyte decomposition, and materials' activation during cycling.[27–29]

Figure 6b illustrates the cycling stability performance of metallic MoS_2 nanotube under the current density of 2 A g^{-1}. As shown in Figure 6b, the pure metallic MoS_2 nanotube electrode delivers a high specific capacity of 1502 mA h g^{-1} at 2 A g^{-1} in the first discharge cycle and rapidly stabilizes at a specific capacity of ≈1000 mA h g^{-1} within 10 cycles. The capacity is kept at around 1000 mA h g^{-1} without any decay for 150 cycles and then starts to increase, which is consistent with the charge–discharge profiles. The batteries were disassembled after 200 cycles to investigate the morphology evolution of the metallic MoS_2 nanotube. TEM image (Figure S6a, Supporting Information) demonstrates that even after 200 cycles, the material still kept their tubular structure, which again confirms that our metallic MoS_2 nanotube is robust for lithium-ion battery application, agreeing with the excellent cycling stability performance.

The rate performance of metallic MoS_2 nanotube and 2H MoS_2 nanosheets is demonstrated in Figure 6c. Under the current densities of 200 mA g^{-1}, 500 mA g^{-1}, 1 A g^{-1}, 2 A g^{-1}, 5 A g^{-1}, 10 A g^{-1}, and 20 A g^{-1}, the pure metallic MoS_2 nanotube electrode exhibits a reversible capacity of ≈1080, 1048, 1020, 978, 875, 725, and 589 mA h g^{-1}, respectively. The electrode regains the capacity of 1121 m Ah g^{-1} for six stable cycles, which is even a little higher than the initial six cycles, upon reduction of the current density back to 200 mA g^{-1}. It is worth noting that even under a high current density of 20 A g^{-1}, our metallic MoS_2 nanotube electrode still provides a high reversible capacity of 589 mA h g^{-1}. In contrast, the rate performance of pure 2H MoS_2 nanosheets electrode was also demonstrated
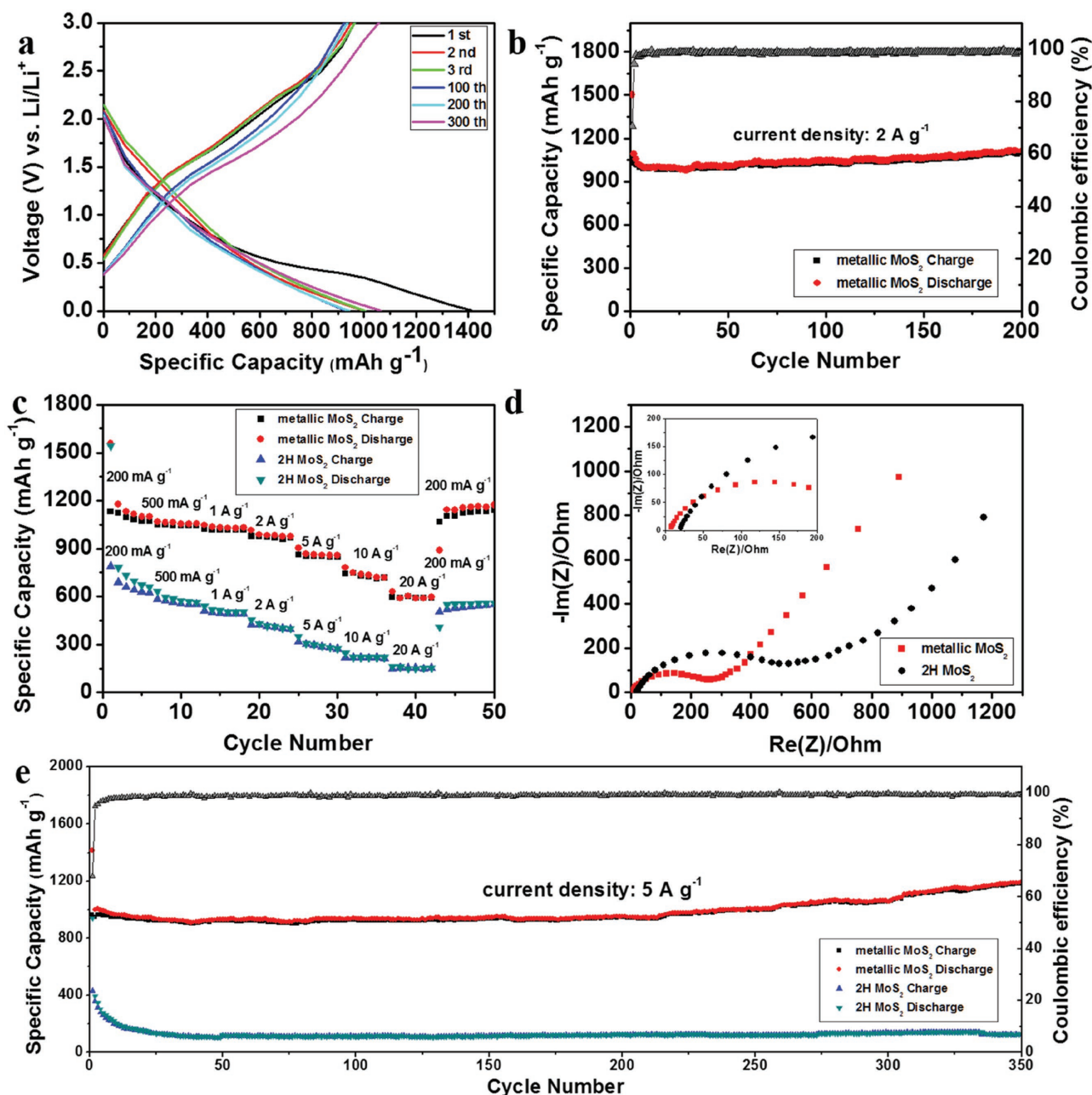
Figure 6. Electrochemical performance of metallic MoS$_2$ nanotube. a) Charge/discharge profiles for the first three and 100th, 200th, and 300th cycles at a current density of 5 A g^{-1}. b) Specific capacity and Coulombic efficiency versus cycle number at a current density of 2 A g^{-1}. c) Rate performance of the metallic MoS$_2$ nanotube electrode and 2H MoS$_2$ nanosheets electrode, and d) electrochemical impedance spectra of metallic MoS$_2$ and 2H MoS$_2$ batteries. e) Cycling performance of metallic MoS$_2$ nanotube electrode and 2H MoS$_2$ electrode at a current density of 5 A g^{-1}.

under the same current densities. As shown in Figure 6c, pure 2H MoS$_2$ electrode delivers the capacities of 631, 556, 494, 410, 270, 210, and 150 mA h g^{-1}, respectively, at current densities of 0.2, 0.5, 1, 2, 5, 10, and 20 A g^{-1}. The pure 2H MoS$_2$ electrode recovers its capacity back to ≈550 mA h g^{-1} when the current density reduces back to 200 mA g^{-1}.

To further explore the driving force for the enhanced rate performance of metallic MoS$_2$ than 2H MoS$_2$ as lithium-ion anode electrode, the electrochemical impedance spectra (EIS) of pure metallic MoS$_2$ nanotube and 2H MoS$_2$ nanosheets electrode are

compared in Figure 6d. The Nyquist plots of the impedance spectrum contain a semicircle in high frequency region and a straight line in low frequency region. The intercept of the semicircle with the Re (Z) axis in the high frequency region presents the Ohmic resistance of the entire cell, whereas the diameter of the semicircle is indicative of the charge transfer resistance. The slope of the straight line in low frequency region is related to the lithium-ion diffusion. The larger slope results from faster lithium-ion diffusion. It is evident that the intercept (inset image in Figure 6d) and diameter of the semicircle of metallic

**ADVANCED
SCIENCE NEWS**
www.advancedsciencenews.com

**ADVANCED
ENERGY
MATERIALS**
www.advenergymat.de

MoS_2 nanotube electrode are much smaller than 2H MoS_2, suggesting a better charge transfer kinetics. Also, the slope of the straight line for metallic MoS_2 is much larger than 2H MoS_2, which confirms the improved lithium-ion diffusion. The lower resistance and better diffusion properties guarantee a much better rate performance of the pure metallic MoS_2 nanotube electrode.

To better demonstrate the cycling stability under high current density, Figure 6e shows the specific capacity and Coulombic efficiency versus cycle number at a current density of 5 A g^{-1} for 350 cycles of the metallic MoS_2 nanotube in a lithium-ion battery. According to the charge/discharge curves, the metallic MoS_2 nanotube electrode exhibits excellent cycling stability and ultrahigh reversible capacity of 935 mA h g^{-1} at the first 200 cycles. The capacity continuously increases to ≈1150 mA h g^{-1} due to the reversible formation of organic polymeric/gel-like layer by electrolyte decomposition and activation of the active materials. The cycling stability of 2H MoS_2 under 5 A g^{-1} is also shown in Figure 6e as a contrast. It displays a much lower capacity of ≈150 mA h g^{-1} after 350 cycles, due to its poor intrinsic conductivity. The outstanding cycling stability and specific capacity under high current density prove that our as-prepared metallic MoS_2 nanotube has the potential to be a good substitute for commercial graphite as the lithium-ion anode. The phase stability of metallic MoS_2 in batteries was also investigated by Raman spectra as shown in Figure S6b (Supporting Information). The spectra exhibit that even after 350 cycles, the typical peaks of J_1 and J_3 for metallic MoS_2 can still be well defined, and no peaks for 2H MoS_2 exist, which proves that there is no obvious phase transfer after 350 cycles.

Compared to the rate performance of current reported MoS_2 on lithium-ion batteries,[2–4,7,9–12,17,22,23,25,30–37] (Table S1, Supporting Information) the pure metallic MoS_2 nanotube electrode shows better rate performance and high reversible capacity under high current density without any additional additives. This exceptional electrochemical performance is ascribed to the vertically assembled unique porous and tubular structure, as well as their high electrical conductivity. The advantages of the metallic MoS_2 nanotube can be presumed in the following aspects: (1) the as-prepared metallic MoS_2 nanotube owns high intrinsic conductivity. This intrinsic conductivity enormously improves the efficiency of ion diffusion and charge transfer during cycling, which results in excellent rate performance especially under very high current densities on lithium-ion batteries. (2) Without adding any carbon sources, the lithium-ions could react with the metallic MoS_2 nanotube directly, avoiding to cross over the carbon material first. This improves the rate performance and decreases the side reactions between lithium-ion and carbon-based materials. (3) The nanotube structure could help to avoid aggregation of MoS_2 and increase the utilization efficiency of intercalation sites that would be beneficial to the cycling stability and specific capacity of the as-prepared material. (4) The vertically assembled porous structure enlarges the contact area of the electrode and electrolyte. It allows the lithium-ion and electrolyte to pass through easily and shortens the distance for ion diffusion and charge transfer. As a result, the rate performance is improved. Overall, such anode material with ultrahigh capacity and excellent rate performance could provide a new direction for researchers to develop high capacity anodes, for various lithium-ion and beyond lithium-ion batteries.

3. Conclusions

In summary, for the first time, the metallic porous nanotube assembled with vertically aligned metallic MoS_2 was synthesized in an environmentally friendly solvent, ethanol, with the scalable solvothermal method. The pure nanotube was subsequently investigated as a carbon-free, binder-free anode electrode for lithium-ion batteries. This unique metallic MoS_2 nanotube structure delivers an ultrahigh electrochemical performance with a reversible capacity of ≈1100 mA h g^{-1} under the high current density of 5 A g^{-1} even after 350 cycles. In addition, without any additional conductive additives, the metallic MoS_2 nanotube structure can still exhibit an extremely high reversible capacity of 589 mA h g^{-1} under a ultrahigh current density of 20 A g^{-1}, owing to its high intrinsic conductivity and the unique porous tubular structure with well-aligned building blocks. The tubular structure also attributes to prevent the aggregation of MoS_2 nanosheets, which improves the cycle stability of the electrode. Furthermore, the presence of the unique peak of metallic MoS_2 at 1.5 V on the anodic scan of the CV curves was firstly figured out and investigated in this study, leading to a probable evaluation standard for metallic MoS_2. The material fabrication strategy and structural design approach could also be promoted for the modification of other 2D layered materials and shed light on the corresponding applications in high-performance energy storage and energy conversion.

4. Experimental Section

Metallic MoS_2 Nanotube Preparation: In a typical synthesis of the metallic MoS_2 nanotube, MoO_3 (18 mg, Fisher Scientific, USA), thioacetamine (21 mg, Sigma-Aldrich, USA), and urea (0.15 g, Sigma-Aldrich, USA) were dissolved in ethanol (15 mL) and stirred for 1 h. Then one piece of AAO was added into the solution before the solution was transferred to an autoclave. The autoclave was kept in a furnace for 16 h at 200 °C. After cooling to room temperature, the AAO piece embedded with metallic MoS_2 nanotube was taken out and washed with ethanol for three times. The AAO piece was etched away by acid under room temperature, and the resulted MoS_2 nanotube was suspended in ethanol for stabilization.

2H MoS_2 Nanosheets Preparation: For the synthesis of the semiconducting 2H MoS_2, the same amounts of MoO_3, thioacetamine, and urea were dissolved in water (15 mL) and stirred for 1 h before transferring to an autoclave. The autoclave was kept in a furnace for 24 h at 240 °C. The as-prepared 2H MoS_2 was washed with ethanol for three times and then stabilized in ethanol.

Structural and Physical Characterization: The morphology of the as-prepared MoS_2 was characterized by the SEM (Hitachi S4800) and TEM (JEOL 1010). XPS was conducted using the Thermo Scientific K-Alpha XPS (ESCA) system. The vacuum of the chamber was 8×10^{-8} mBar. Raman spectroscopy was carried out on a LabRam HR800 UV NIR with 532 nm laser excitation. X-ray diffraction (PANalytical/Philips X'Pert Pro) patterns of MoS_2 were recorded for two θ values ranging from 5° to 60° with Cu Kα radiation.

Electrochemical Measurement: Standard CR2025-type coin cells were assembled to measure the electrochemical performance of the as-synthesized metallic MoS_2 nanotube. The metallic MoS_2 nanotube

electrodes were directly assembled into the coin cells in an argon-filled glove box, using 1M LiPF$_6$/ethylene carbonate and dimethyl carbonate (1:1 vol/vol) as an electrolyte, with 1% fluoroethylene carbonate additive. CV and EIS were measured using a biologic SP-150. Galvanostatic charge–discharge tests were performed on a multichannel battery testing system (Land CT2001A).

Supporting Information

Supporting Information is available from the Wiley Online Library or from the author.

Conflict of Interest

The authors declare no conflict of interest.

[1] M. Chhowalla, H. S. Shin, G. Eda, L. J. Li, K. P. Loh, H. Zhang, *Nat. Chem.* **2013**, *5*, 263.

[2] K. Chang, W. X. Chen, *ACS Nano* **2011**, *5*, 4720.

[3] H. Hwang, H. Kim, J. Cho, *Nano Lett.* **2011**, *11*, 4826.

[4] K. Chang, D. S. Geng, X. F. Li, J. L. Yang, Y. J. Tang, M. Cai, R. Y. Li, X. L. Sun, *Adv. Energy Mater.* **2013**, *3*, 839.

[5] X. S. Zhou, L. J. Wan, Y. G. Guo, *Chem. Commun.* **2013**, *49*, 1838.

[6] G. D. Du, Z. P. Guo, S. Q. Wang, R. Zeng, Z. X. Chen, H. K. Liu, *Chem. Commun.* **2010**, *46*, 1106.

[7] S. P. Zhang, B. V. R. Chowdari, Z. Y. Wen, J. Jin, J. H. Yang, *ACS Nano* **2015**, *9*, 12464.

[8] X. Geng, W. Sun, W. Wu, B. Chen, A. Al-Hilo, M. Benamara, H. Zhu, F. Watanabe, J. Cui, T. P. Chen, *Nat. Commun.* **2016**, *7*, 10672.

[9] M. Wu, J. Zhan, K. Wu, Z. Li, L. Wang, B. Geng, L. Wang, D. Pan, *J. Mater. Chem.* **2017**, *5*, 14061.

[10] F. Zhou, S. Xin, H. W. Liang, L. T. Song, S. H. Yu, *Angew. Chem., Int. Ed.* **2014**, *53*, 11552.

[11] Y. Q. Teng, H. L. Zhao, Z. J. Zhang, Z. L. Li, Q. Xia, Y. Zhang, L. N. Zhao, X. F. Du, Z. H. Du, P. P. Lv, K. Swierczek, *ACS Nano* **2016**, *10*, 8526.

[12] Y. M. Chen, X. Y. Yu, Z. Li, U. Paik, X. W. Lou, *Sci. Adv.* **2016**, *2*, e1600021.

[13] X. M. Geng, Y. L. Zhang, Y. Han, J. X. Li, L. Yang, M. Benamara, L. Chen, H. L. Zhu, *Nano Lett.* **2017**, *17*, 1825.

[14] M. A. Lukowski, A. S. Daniel, F. Meng, A. Forticaux, L. S. Li, S. Jin, *J. Am. Chem. Soc.* **2013**, *135*, 10274.

[15] M. Acerce, D. Voiry, M. Chhowalla, *Nat. Nanotechnol.* **2015**, *10*, 313.

[16] Q. Liu, Q. Fang, W. S. Chu, Y. Y. Wan, X. L. Li, W. Y. Xu, M. Habib, S. Tao, Y. Zhou, D. B. Liu, T. Xiang, A. Khalil, X. J. Wu, M. Chhowalla, P. M. Ajayan, L. Song, *Chem. Mater.* **2017**, *29*, 4738.

[17] T. Xiang, Q. Fang, H. Xie, C. Q. Wu, C. D. Wang, Y. Zhou, D. B. Liu, S. M. Chen, A. Khalil, S. Tao, Q. Liu, L. Song, *Nanoscale* **2017**, *9*, 6975.

[18] Z. T. Shi, W. P. Kang, J. Xu, Y. W. Sun, M. Jiang, T. W. Ng, H. T. Xue, D. Y. W. Yu, W. J. Zhang, C. S. Lee, *Nano Energy* **2016**, *22*, 27.

[19] L. X. Zheng, S. C. Han, H. Liu, P. P. Yu, X. S. Fang, *Small* **2016**, *12*, 1527.

[20] X. Q. Xie, T. Makaryan, M. Q. Zhao, K. L. Van Aken, Y. Gogotsi, G. X. Wang, *Adv. Energy Mater.* **2016**, *6*, 1502161.

[21] Y. Jing, E. O. Ortiz-Quiles, C. R. Cabrera, Z. F. Chen, Z. Zhou, *Electrochim. Acta* **2014**, *147*, 392.

[22] T. L. Wang, C. L. Sun, M. Z. Yang, G. Zhao, S. Z. Wang, F. K. Ma, L. Zhang, Y. L. Shao, Y. Z. Wu, B. B. Huang, X. P. Hao, *J. Alloys Compd.* **2017**, *716*, 112.

[23] Y. F. Chao, R. Jalili, Y. Ge, C. Y. Wang, T. Zheng, K. W. Shu, G. G. Wallace, *Adv. Funct. Mater.* **2017**, *27*, 1700234.

[24] J. Xiao, X. J. Wang, X. Q. Yang, S. D. Xun, G. Liu, P. K. Koech, J. Liu, J. P. Lemmon, *Adv. Funct. Mater.* **2011**, *21*, 2840.

[25] Y. P. Liu, X. Y. He, D. Hanlon, A. Harvey, U. Khan, Y. G. Li, J. N. Coleman, *ACS Nano* **2016**, *10*, 5980.

[26] Y. C. Lin, D. O. Dumcencon, Y. S. Huang, K. Suenaga, *Nat. Nanotechnol.* **2014**, *9*, 391.

[27] X. H. Wu, Z. Y. Wang, M. Z. Yu, L. Y. Xiu, J. S. Qiu, *Adv. Mater.* **2017**, *29*, 1607017.

[28] Y. F. Shi, B. K. Guo, S. A. Corr, Q. H. Shi, Y. S. Hu, K. R. Heier, L. Q. Chen, R. Seshadri, G. D. Stucky, *Nano Lett.* **2009**, *9*, 4215.

[29] Z. Y. Wang, J. S. Chen, T. Zhu, S. Madhavi, X. W. Lou, *Chem. Commun.* **2010**, *46*, 6906.

[30] J. Wang, J. L. Liu, D. L. Chao, J. X. Yan, J. Y. Lin, Z. X. Shen, *Adv. Mater.* **2014**, *26*, 7162.

[31] J. W. Zhou, J. Qin, X. Zhang, C. S. Shi, E. Z. Liu, J. J. Li, N. Q. Zhao, C. N. He, *ACS Nano* **2015**, *9*, 3837.

[32] Y. Fang, Y. Y. Lv, F. Gong, A. A. Elzatahry, G. F. Zheng, D. Y. Zhao, *Adv. Mater.* **2016**, *28*, 9385.

[33] J. Y. Li, Y. Hou, X. F. Gao, D. S. Guan, Y. Y. Xie, J. H. Chen, C. Yuan, *Nano Energy* **2015**, *16*, 10.

[34] H. Jiang, D. Y. Ren, H. F. Wang, Y. J. Hu, S. J. Guo, H. Y. Yuan, P. J. Hu, L. Zhang, C. Z. Li, *Adv. Mater.* **2015**, *27*, 3687.

[35] D. B. Kong, H. Y. He, Q. Song, B. Wang, W. Lv, Q. H. Yang, L. J. Zhi, *Energy Environ. Sci.* **2014**, *7*, 3320.

[36] F. Y. Xiong, Z. Y. Cai, L. B. Qu, P. F. Zhang, Z. F. Yuan, O. K. Asare, W. W. Xu, C. Lin, L. Q. Mai, *ACS Appl. Mater. Interfaces* **2015**, *7*, 12625.

[37] L. C. Yang, S. N. Wang, J. J. Mao, J. W. Deng, Q. S. Gao, Y. Tang, O. G. Schmidt, *Adv. Mater.* **2013**, *25*, 1180.